Comprehensive Approach for Correction of Motion and Distortion in Diffusion-Weighted MRI

G.K. Rohde,[1,3]* A.S. Barnett,[2] P.J. Basser,[1] S. Marenco,[2] and C. Pierpaoli[1]

Patient motion and image distortion induced by eddy currents cause artifacts in maps of diffusion parameters computed from diffusion-weighted (DW) images. A novel and comprehensive approach to correct for spatial misalignment of DW imaging (DWI) volumes acquired with different strengths and orientations of the diffusion sensitizing gradients is presented. This approach uses a mutual information-based registration technique and a spatial transformation model containing parameters that correct for eddy current-induced image distortion and rigid body motion in three dimensions. All parameters are optimized simultaneously for an accurate and fast solution to the registration problem. The images can also be registered to a normalized template with a single interpolation step without additional computational cost. Following registration, the signal amplitude of each DWI volume is corrected to account for size variations of the object produced by the distortion correction, and the *b*-matrices are properly recalculated to account for any rotation applied during registration. Both qualitative and quantitative results show that this approach produces a significant improvement of diffusion tensor imaging (DTI) data acquired in the human brain.   Magn Reson Med 51:103–114, 2004. Published 2003 Wiley-Liss, Inc.[†]

Key words: image registration; mutual information; distortion correction; motion correction; eddy currents

MRI measurements of water diffusion provide important information about compositional, structural, and organizational features of biological tissues. Most clinical MRI diffusion studies are performed by acquiring single-shot echo-planar images (EPI) with diffusion sensitizing gradients of different strengths and orientations. In diffusion tensor imaging (DTI) (1), at least seven images must be acquired: one image with no diffusion sensitization, and six diffusion-weighted (DW) images with diffusion sensitization in noncollinear directions. DTI analyses, in addition to other approaches used to extract diffusion information from MRI data (2–5), require the different DW images to be spatially coregistered.

Unfortunately, eddy current-induced image distortions and patient motion during prolonged acquisitions cause misalignment of the DW images. Eddy currents are significantly reduced, but not eliminated, by actively shielded gradients (6) and preemphasis correction schemes (7) in modern magnets. The methods that have been proposed to reduce residual eddy current-induced distortions in DW images are based on either field maps or images.

In a field map-based correction scheme, such as that presented by Jezzard et al. (8), one measures the magnetic field produced by the eddy currents and then corrects the distortion using the field map and theoretical models of how field inhomogeneities distort the images. The major obstacle to implementation is the difficulty of rapidly acquiring reliable field maps.

In an image-based registration scheme, one uses a cost function Q to measure how well the images are spatially aligned. First, a target image is chosen as a reference for all other images in the data set (source images). Because it is usually less distorted and has a higher signal-to-noise ratio (SNR) than the heavily DW images, the image acquired with no diffusion sensitization (the T_2-weighted image), is usually used as the target image for registering DW images. Next, using a spatial transformation model, one aligns all other images to the target image by optimizing a cost function. Image-based registration schemes differ from each other in terms of 1) the definition of Q, 2) the types of transformations applied to the image in searching for the maximum of Q, and 3) the numerical optimization method used in searching for the maximum of Q. We chose to work with an image-based registration scheme because a field map, which is usually not available for DW images acquired on conventional clinical scanner, is not required. In addition, an image-based scheme allows one to correct for misregistration produced by subject motion.

Haselgrove and Moore (9) proposed the first image-based registration method to correct for eddy current-induced distortions. They used the undistorted T_2-weighted image as a target image for the registration of the DW images. Q was based on the cross correlations between the source image and the target image. Unfortunately, cross correlation performs poorly as a measure of alignment when the contrast of the source and target images differs significantly. Experiments by Bastin et al. (10) indicate that this approach does not perform well in registering T_2-weighted images to DW images acquired with *b*-values higher than 300 s mm^{-2} (10).

Cost functions based on mutual information are more robust than those based on correlation for registering images with significantly different contrast. A mutual information-based method was presented by Horsfield (11), who proposed that the effect of eddy currents could be measured by registering DW images acquired on a special phantom with low diffusivity and nonuniform relaxation properties. The correction parameters computed from the phantom could in turn be used to correct anatomical DW images acquired in the same scanner with the same sequence, provided that 1) the subject's position in the scan-

ner is sufficiently well known, and 2) gradient performance is stable over time.

Andersson and Skare (12) recently proposed a scheme that uses the goodness-of-fit of the apparent diffusion tensor (**D**) calculation for guiding the image registration process. They define Q using the goodness-of-fit (χ^2) of the DW imaging (DWI) signal to the b-matrix (1). This interesting approach has the advantage of correcting for both eddy current-induced distortions and subject motion. However, as the authors pointed out, this method can not be used to register DW images to T_2-weighted images when a single level of diffusion weighting is sampled because, in this case, the T_2-weighted images do not contribute to χ^2.

Surprisingly, until recently (12), misregistration from patient motion has been neglected as a potential source of artifacts in diffusion MRI studies, although it has been long recognized as such in functional MRI studies.

The goal of this work was to design a robust image registration approach that would correct the spatial misregistration of DWI volumes[1] originating from both subject motion and eddy current-induced distortions. Our postprocessing method can also be used to position the dataset in a standardized orientation. The b-matrix and the signal magnitude of each DWI volume are recalculated to take into account the effects of the spatial transformation applied. The method requires only one image interpolation step and thus avoids unnecessary blurring of the images, without requiring additional measurements on phantoms or additional scans to map the magnetic field produced by the eddy currents.

MATERIALS AND METHODS

In this section, we first describe the pulse sequence and the acquisition parameters we used. We then present a mathematical formulation of the registration problem. We describe the spatial transformation **f**, the cost function Q, the numerical method for finding the model parameters that maximize Q, and the postregistration processing necessary to correct the image brightness and to rotate the b-matrices. Finally, we describe the experimental design and data analysis approach for the tests we performed to validate our results.

Pulse Sequence and MRI Parameters

We designed our correction scheme to reduce artifacts in data sets acquired with a standard single-shot, multislice, spin-echo EPI sequence (i.e., fat suppression pulse, 90° pulse, first diffusion gradient, 180° pulse, second diffusion gradient, and EPI readout). The acquisition order is shown in Fig. 1. We begin with a dummy scan, acquired with no radiofrequency (RF) excitation, which permits us to correct for the direct current offset of the RF amplifier. Next, we acquire an EPI reference scan for each slice. Finally, we collect the image data looping through all slices and the
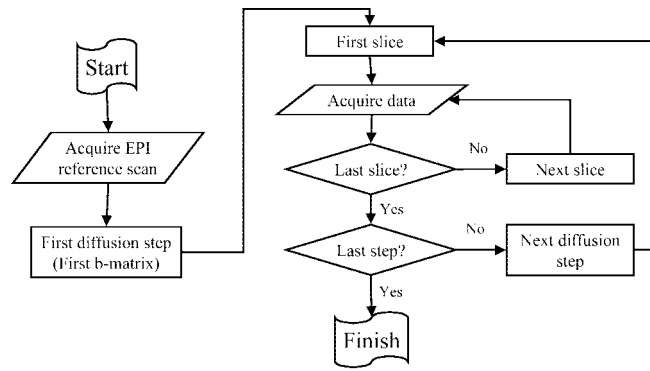

FIG. 1. Block diagram description of the volume acquisition procedure.

different diffusion weightings. The slice loop is the innermost loop, so we acquire all slices composing a volume before proceeding to the next diffusion weighting.

Scans were performed on a 1.5 T GE Signa system equipped with a whole-body gradient coil able to produce gradient pulses up to 50 mT/m (GE Medical Systems, Milwaukee, WI). We scanned a cylindrical silicone oil phantom and the brains of healthy subjects. The preemphasis correction for eddy currents provided by the system manufacturer was disabled in some scans to obtain images with severe geometric distortions. Some imaging parameters, such as resolution, repetition time (TR), total number of images, etc., varied slightly for the different tests we performed. For brevity, we report the imaging parameters of the brain study shown in Figs. 6–9. The imaged volume was composed of 80 contiguous slices with 2-mm slice thickness and 2-mm in-plane resolution. The TE was 82.7 ms, the readout time was 50 ms, and the TR was >10 s with cardiac gating (four acquisitions per heartbeat, starting with a 150-ms delay after the rise of the sphygmic wave as measured with a peripheral pulse oxymeter). The gradient strength was 49 mT/m, yielding a b-value (i.e., trace of the b-matrix) of 1120 s/mm^2. A total of 56 3D images were acquired by repeating eight times a previously described (23) diffusion sampling scheme, which includes one volume with no diffusion weighting followed by the same volume six times, acquired with diffusion gradients applied in different directions. The total imaging time was approximately 20 min. Replicate volumes were acquired for signal-to-noise ratio (SNR) considerations in order to improve the quality of the estimated diffusion tensor parameters.

Formulation of the Spatial Transformation Model

A data set from a diffusion MR study consists of multiple volumes acquired with different strengths and orientations of the diffusion sensitizing gradients. To register a set of images or 3D volumes, we first define a target coordinate system **x**. We then define a source coordinate system $\mathbf{x}_\alpha$ for each volume α. The registration problem consists of finding the coordinate transformation $\mathbf{f}_\alpha(\mathbf{x})$ for each volume α that transforms the target coordinates **x** into the source coordinates $\mathbf{x}_\alpha$. We describe the transformations with a set

---

[1]Here and throughout this work we use the term "volume" to identify a set of slices acquired with identical acquisition parameters covering the imaged object without gaps. Different "volumes" do not differ in their spatial coverage of the object, but do differ in the strength and/or orientation of the diffusion sensitizing gradients used to acquire them.

of parameters $\mathbf{p}_\alpha = \{ p_\alpha^1, p_\alpha^2, \ldots, p_\alpha^m \}$, where m is the total number of parameters:

$$\mathbf{x}_\alpha = \mathbf{f}_\alpha(\mathbf{x}) = \mathbf{f}(\mathbf{x}; \mathbf{p}_\alpha) \qquad [1]$$

We then define a cost function Q that depends upon the image values and the parameters $\mathbf{p}_\alpha$. We then find $\mathbf{f}$ by finding $\mathbf{p}_\alpha$ for which Q is an extremum.

The first T_2-weighted volume acquired is extracted from the DWI dataset and rigidly registered to a standard template. Subsequent registrations of each DW image to the normalized T_2-weighted target volume will then cause then entire DWI dataset to be positioned in a standardized orientation. All of the human brain images displayed in this work were spatially normalized using this method. Although this volume is free from eddy current-induced distortions, it contains geometrical distortions due to $\mathbf{B}_0$ inhomogeneity caused by the magnetic susceptibility of the object. These distortions are generally accompanied by localized changes in the brightness of the image. Because these distortions and brightness modulations are the same in both T_2-weighted and DW images, they do not cause misregistration artifacts in the computed diffusion parameters. However, if large corrections of the shape of the object (in particular magnification) are required to correct the DW images for eddy-current distortion, one should also correct their brightness (signal magnitude) appropriately to account for changes in size of the object. Neglecting to correct the brightness of the DW images following distortion correction will result in errors in the computed diffusion parameters.

Each volume α consists of a 3D array of pixel values, $I_\alpha[p,q,r]$, where p, q, and r are the array indices. We define the image coordinates for volume α as

$$\mathbf{x}_\alpha = (x_{1\alpha}, x_{2\alpha}, x_{3\alpha}) = (s_1 p, s_2 q, s_3 r) \qquad [2]$$

where s_1 and s_2 are the nominal in-plane pixel sizes, and s_3 is the slice separation. Each volume $I_\alpha[p,q,r]$ is only defined for integral values of the indices p, Q, and r. We use trilinear interpolation (13) to define a continuous function $I_\alpha(\mathbf{x}_\alpha)$ in terms of the measured values $I_\alpha[p,q,r]$.

Call the coordinate system of the target image $\mathbf{x}$. For each volume α we seek the properly registered and brightness-corrected image I_α^r. As shown in Eq. [8], I_α^r is related to the measured image I_α by the equation

$$I_\alpha^r(\mathbf{x}) = I_\alpha(\mathbf{f}_\alpha(\mathbf{x}))\boldsymbol{\Gamma}_\alpha(\mathbf{f}_\alpha(\mathbf{x})), \qquad [3]$$

where $\mathbf{f}_\alpha$ is a coordinate transformation, and $\Gamma_\alpha(\mathbf{x})$ is a brightness correction function. We propose a parameterized form for $\mathbf{f}_\alpha$ that can correct for patient motion and eddy current-induced distortion. We find the best values of the parameters by maximizing the cost function Q as described below. Since the brightness correction is a function of the spatial transformation necessary to correct for eddy current-induced distortions, we can express the brightness correction $\Gamma_\alpha(\mathbf{x})$ in terms of parameters we used to model the eddy current field (see Effects of Eddy Currents section below).

We decompose the spatial transformation $\mathbf{f}$ into two steps. The first step describes the change in location and orientation of the object between acquisition times of the two volumes, and the second step describes the distortion introduced by the acquisition process.

We model the patient's brain as a rigid body, and describe its displacement and change in orientation by the equation

$$\mathbf{y}_\alpha = \mathbf{R}\mathbf{x} + \mathbf{a} \qquad [4]$$

where $\mathbf{R}$ is a rotation matrix, $\mathbf{a}$ is a displacement vector, and $\mathbf{y}_\alpha$ is an intermediate set of coordinates that describes the orientation of the patient's head at the time of the acquisition of volume α. Equation [4] contains six parameters: the three components of the displacement vector $\mathbf{a}$, and three parameters (typically Euler angles ϕ, θ, and ψ) that define the rotation $\mathbf{R}$ (14). No changes in the image brightness are associated with this transformation.

Subject motion between the start of the excitation pulse and the end of the data acquisition can potentially affect the data in a significant way. For a single-shot EPI acquisition, this period lasts about 1.5 TE, or about 120 ms in our case. Head motion during this period has two effects on the data: 1) The component of velocity parallel to the diffusion sensitizing gradients causes a phase shift in the reconstructed image. This phase shift does not cause any artifact in EPI single-shot magnitude images. 2) Motion during the readout can cause blurring. An image registration algorithm is clearly not appropriate for correcting image blurring.

Effects of Eddy Currents

The image distortion due to eddy currents depends on the time and space dependence of $b_{eddy}(\mathbf{y}_\alpha,t)$, the component parallel to $\mathbf{B}_0$ of the magnetic field generated by the eddy currents. The shifts in the readout, phase-encode, and slice-select directions are:

$$\delta_{read} = \frac{b_{eddy}}{g_{readout}s_1} \cong \frac{b_{eddy}}{7\,gauss} \qquad [5]$$

$$\delta_{phase} = \frac{b_{eddy}\boldsymbol{\tau}_{echo}}{G_{blip}s_2} \cong \frac{b_{eddy}}{.07\,gauss} \qquad [6]$$

$$\delta_{slice} = \frac{b_{eddy}}{g_{slice}s_3} \cong \frac{b_{eddy}}{2.5\,gauss} \qquad [7]$$

where δ_{read} and δ_{phase} are in pixels; δ_{slice} is multiples of the slice thickness; G_{blip} is the area of the phase-encode blips; τ_{echo} is the time between consecutive echoes in the readout echo train; s_1, s_2, and s_3 are defined in Eq. [2]; and the numerical values are typical of the scans we perform. We can safely ignore the shifts in the readout and slice-select directions, as they are almost two orders of magnitude smaller than the shifts in the phase-encode direction. If $b_{eddy}(\mathbf{y}_\alpha,t)$ were to change appreciably during the readout phase of image acquisition, the image would suffer blurring that cannot be corrected by a simple coordinate transformation.

As shown in the Appendix, if we assume that $b_{eddy}(\mathbf{y}_\alpha, t)$ is approximately constant during the readout, and that eddy current fields from the acquisition of one slice do not interfere with the next, the pixel values for volume α are

$$I_\alpha[m, l, q] = \tilde{W}_\alpha(ms_1, ls_2 - \beta b_{eddy}(ms_1, ls_2, qs_3), qs_3)$$
$$\times \left(1 + \frac{\partial(\beta b_{eddy})}{\partial y_2} \right) \quad [8]$$

where $\tilde{W}_\alpha$ is the undistorted image of volume α smoothed by the point spread function (PSF) of the imaging system, and β is given in Eq. [A3]. Comparing Eqs. [8] and [3], we conclude that the transformation and brightness correction associated with eddy currents are

$$\mathbf{x}_\alpha = \mathbf{y}_\alpha - \beta b_{eddy} \mathbf{e}_2 \quad [9]$$

with $\mathbf{e}_2 = (0,1,0)$ representing the phase-encode direction and

$$\Gamma_\alpha(\mathbf{x}_\alpha) = \left(1 + \frac{\partial(\beta b_{eddy})}{\partial y_2} \right)_{\mathbf{x}_\alpha = \mathbf{y}_\alpha}. \quad [10]$$

We now have to model b_{eddy}. Since we can neglect the fields due to eddy currents induced in the patient's head, $b_{eddy}(\mathbf{y}_\alpha, t)$ in the imaging volume obeys Laplace's equation (15)

$$\nabla^2 b_{eddy} = 0. \quad [11]$$

Expanding the solution of Laplace's equation in Cartesian coordinates up to second order, we approximate b_{eddy} by

$$\beta b_{eddy}(\mathbf{y}_\alpha) = [c_0 + c_1 y_{\alpha 1} + c_2 y_{\alpha 2} + c_3 y_{\alpha 3} + c_4 y_{\alpha 1} y_{\alpha 2} + c_5 y_{\alpha 1} y_{\alpha 3}$$
$$+ c_6 y_{\alpha 2} y_{\alpha 3} + c_7 (y_{\alpha 1}^2 - y_{\alpha 2}^2) + c_8 (2 y_{\alpha 3}^2 - y_{\alpha 1}^2 - y_{\alpha 2}^2)] \quad [12]$$

where $c_0 - c_8$ are parameters to be determined from the optimization procedure. We can use Eq. [12] to write the brightness correction function in terms of the fit parameters:

$$\Gamma_\alpha = 1 + c_2 + c_4 y_{\alpha 1} + c_6 y_{\alpha 3} + 2(c_7 + c_8) y_{\alpha 2}. \quad [13]$$

Equations [4], [9], and [12] define the transformation $\mathbf{f}_\alpha$ from target coordinates $\mathbf{x}$ to the source coordinates $\mathbf{x}_\alpha$. This transformation is not unique, however, because the c_0 and t_2 are not independent. We therefore set $c_0 = 0$ without loss of generality, and are left with 14 parameters: eight (c1–c8) that describe the eddy current distortion, and six (a_1, a_2, a_3, ϕ, θ, and ψ) that describe the rigid body displacement of the object.

As mentioned previously, very short time constant eddy currents (i.e., eddy currents with significant variation during the readout period) do not produce image distortion, but rather image blurring that cannot be corrected by image registration. Our approach will correct for the effect of eddy currents that have relatively long time constants with negligible decay during the readout period. However, our 3D correction model assumes that the eddy-current field is the same for all of the slices in a particular volume. This assumption requires either that the eddy currents from the previous excitation have died away during the time interval between consecutive excitations or that a steady state is reached. In the latter case, the first few slices acquired in each volume after the gradient direction has changed will be collected before the steady state is reached, and will have an amount of distortion inconsistent with that accounted for by our model. We performed a set of 2D registration experiments on a silicone oil phantom in order to investigate this effect on our magnet.

Cost Function

In image registration problems, the goal of the cost function Q is to measure how well two images are aligned. It is common to assume that the images are optimally aligned when the statistical dependence between their intensity values is highest. As mentioned earlier, the correlation coefficient is a poor measure of image alignment when the intensities in the images are not linearly related (see Results section). A more robust way of measuring spatial alignment in medical images is to use the mutual information, a special case of the Kullback-Leibler measure (16), between the intensity values of the images to be registered (17–19). The mutual information similarity measure has been shown to be significantly more robust than the correlation coefficient and some other measures of similarity, when images of different modalities are registered (20). In practice, we elected to use the normalized mutual information (21) in our registration program, as it has been shown to avoid any dependency on the amount of image overlap.

Consider two volumes, S and T. The normalized mutual information is defined in terms of three quantities: the normalized histogram $p_S(n)$ of pixel values in volume S, the normalized histogram $p_T(m)$ of pixel values of image T, and the normalized joint histogram $p_{ST}(n,m)$ of pixel values in volume T and the corresponding pixel in image S. Let v_{min} and v_{max} be the minimum and maximum pixel values in volume S, respectively, and let w_{min} and w_{max} be the minimum and maximum pixel values in image T, respectively. We divide the range of pixel values of volume S into N bins of equal width, and the range of pixel values in image T into M bins of equal width. The limits of bin l for volume S are v_l and v_{l+1}, given by

$$v_l = v_{min} + l \frac{v_{max} - v_{min}}{N}, \quad [14]$$

and the limits of bin m for image T are w_m and w_{m+1}, given by

$$w_m = w_{min} + m \frac{w_{max} - w_{min}}{M}. \quad [15]$$

Let n_{Sl} be the number of pixels in volume S with value h in the range $v_l \leq h < v_{l+1}$, n_{Tm} the number of pixels in image T with value d in the range $w_m \leq d < w_{m+1}$, n_{SlTm} the number of voxels for which the value h in volume S lies in the range $v_l \leq h < v_{l+1}$ and the value of the

corresponding voxel in image T lies in the range $w_m \leq d < w_{m+1}$, and let n_{tot} be the total number of voxels in volume S (= the total number of voxels in image T). The normalized histogram of volume S is then

$$p_s(n) = \frac{n_{Sl}}{(n_{tot})},$$ [16]

the normalized histogram of image T is

$$p_T(m) = \frac{n_{Tm}}{(n_{tot})},$$ [17]

and the normalized joint histogram of volumes T and S is

$$p_{ST}(l, m) = \frac{n_{SlTm}}{(n_{tot})}$$ [18]

Our cost function Q is defined in terms of the above histograms by the formula

$$Q(S, T) = \frac{\sum_l p_S(l)\ln(p_S(l)) + \sum_l p_T(m)\ln(p_T(m))}{\sum_m \sum_l p_{ST}(l, m)\ln(p_{ST}(l, m))}.$$ [19]

Lastly, note that the images reconstructed from an MRI experiment often contain intensity spikes. That is why, in practice, we do not choose v_{max} and w_{max} to be the maximum of images T and S, respectively. Instead, we sort the pixels of T by increasing intensity, and choose w_{max} to be some ith (with I some low integer) value from the last element in the sorted list. The same operation is performed to compute v_{max}.

Optimization

To register a source volume α to the target volume T, we have to find the values of the 14 parameters $\mathbf{p}_\alpha = (c_1, c_2, c_3, c_4, c_5, c_6, c_7, c_8, a_1, a_2, a_3, \phi, \theta,$ and $\psi)$ for which $Q(S(\mathbf{f}(\mathbf{x}; \mathbf{p}_\alpha), T(\mathbf{x}))$ in Eq. [19] is a maximum when we use the target volume for volume T and Eqs. [3], [4], [9], and [12] to compute the volume S from the measured volume α. To speed up the registration, we do not apply the brightness correction Γ_α during the optimization process. We use a simple gradient ascent optimization procedure coupled with a golden section line optimization method to maximize Q (13). That is, the registration parameters are searched iteratively according to the equation

$$\mathbf{p}_\alpha^{k+1} = \mathbf{p}_\alpha^k + \varsigma \nabla_{\mathbf{p}_\alpha} Q(\mathbf{p}_\alpha^k),$$ [20]

where ς is determined via the golden section line optimization method (note the change in notation: $Q(S(\mathbf{f}(\mathbf{x}; \mathbf{p}_\alpha), T(\mathbf{x})) = Q(\mathbf{p}_\alpha)$). We evaluate the gradient of the cost function with respect to registration parameters $\mathbf{p}_\alpha$ numerically using finite differences, and several step sizes are used throughout the registration procedure. Note that because different sets of parameters in $\mathbf{p}_\alpha$ have different units and thus affect the value of $Q(\mathbf{p}_\alpha)$ differently, we use Eq.

[20] to determine different sets of parameters in $\mathbf{p}_\alpha$ separately. That is, Eq. [20] is used to update the translation parameters first, followed by the rotation parameters, the linear deformation parameters, and finally the quadratic deformation parameters. The loop is repeated until the improvements in the cost function value fall bellow a chosen tolerance ϵ (typically $\epsilon = 0.0001$). The algorithm also works in multiple resolutions, in a coarse to fine fashion, in order to avoid local optima and decrease computation time.

Postregistration Processing

Intensity Correction

After we register the volume to the target, we apply the brightness correction Γ_α. An example demonstrating the benefit of the brightness correction is shown in the Results section.

b-Matrix Reorientation

Each DWI volume is accompanied by a *b*-matrix that describes its diffusion weighting. In principle, both patient motion and eddy currents can cause errors in the calculation of parameters that describe diffusion in each voxel of a DWI dataset. We use dimensional analysis to estimate the change in the *b*-matrix due to the eddy currents, and to demonstrate that it is very small in normal conditions. The elements of the *b*-matrix scale as

$$b \propto \gamma^2 g_{diff}^2 \tau^3$$ [21]

where γ is the gyro-magnetic ratio, g_{diff} is the strength of the diffusion gradients, and τ is a characteristic time for the experiment. The presence of an eddy current b_{eddy} would change the *b*-value to $\gamma^2 \left| g_{diff} + \frac{b_{eddy}}{L} \right|^2 \tau^3$, resulting in a fractional change in b of $\frac{2b_{eddy}}{g_{diff}L}$, where L is a characteristic length scale over which b_{eddy} varies. For our machine, with pixel shifts of the order of 1–2 pixels, over a 22-cm FOV, $b_{eddy} \approx .1$ gauss, $L \approx 20$ cm, and $g_{diff} \approx 4$ gauss/cm, resulting in a fractional change in the *b*-value of about 0.25%, which we can safely neglect.

However, we do correct for patient motion. The *b*-matrix is calculated with respect to the $\mathbf{y}_\alpha$-coordinates, which are fixed with respect to the scanner. We have to rotate the *b*-matrix to target coordinates $\mathbf{x}$ using the results of the fitting procedure

$$\mathbf{b}' = \mathbf{R}^{-1}\mathbf{b}_\alpha \mathbf{R}$$ [22]

where $\mathbf{b}'$ is the rotated *b*-matrix in target coordinates, $\mathbf{b}_\alpha$ is the computed *b*-matrix, and $\mathbf{R}$ is the rotation matrix defined by the Euler angles ϕ, θ, and ψ obtained from the fitting procedure.

Validation Methods

A common problem one encounters when validating results from image registration algorithms, particularly non-

rigid ones, is the lack of a gold standard. Therefore, we are limited to using indirect measures to establish the reliability of our spatial normalization approach. In this section we describe several approaches we used to establish the reliability of the results produced by our registration algorithm.

Visual Assessment of DW Images and Computed Diffusion Tensor Images

As an initial check, we confirm through visual inspection that the DW images and their corresponding T_2-weighted images are well aligned after registration. Then we check for artifacts in the maps of the computed tensor parameters that could originate from image misalignment in the DWI datasets used to generate them. Often, such artifacts are large enough to be detected at visual inspection of the data. An assumption often used (8,9,11) is that high anisotropy index values around the edges of the brain are associated with image misalignment, because anisotropy in those regions is inconsistent with known anatomy. Following the same approach, we use anisotropy index images, as well as images of the off-diagonal tensor elements, to assess the amount of anisotropic diffusion at the periphery of the brain.

Improved Fitting to the Tensor Model

Andersson and Skare (12) proposed an image registration approach that uses the goodness-of-fit of the apparent diffusion tensor (**D**) calculation to guide the image registration process. Here we use their approach to test the results of our registration algorithm. This scheme relies on the assumption that the DWI data is well described by the tensor model of Basser et al. (1). At the *b*-values we used, this assumption is probably satisfied, although it may not hold true when very large *b*-values are used. Moreover, as mentioned in the Introduction, this approach can only be used to test the registration of different DWI volumes. It does not provide information about the degree of registration of DWI volumes to T_2-weighted volumes.

PCA Analysis of the Data

Several factors contribute to the signal amplitude in each particular voxel of the volumes in a diffusion MRI dataset. These factors include the relaxation and diffusion properties of the tissue, as well as noise. Misregistration artifacts caused by motion and image distortion will affect the signal amplitude by changing the tissue that is imaged at a particular location during different acquisitions. The *n* volumes of a diffusion MRI dataset can be viewed as a random vector **X** of *n* components and *m* elements, where *m* is the number of voxels in the imaged volume. We use the principal component analysis (PCA) described in Ref. 22 to describe the DWI dataset in terms of a new set of *n* uncorrelated volumes (principal components). These principal components are computed as a linear combination of the *n* components of **X** that have special properties in terms of variances of their *m* elements, and they are ordered by decreasing variance. For example, the first principal component is the normalized linear combination (the sum of squares of the coefficients being one) with maxi-
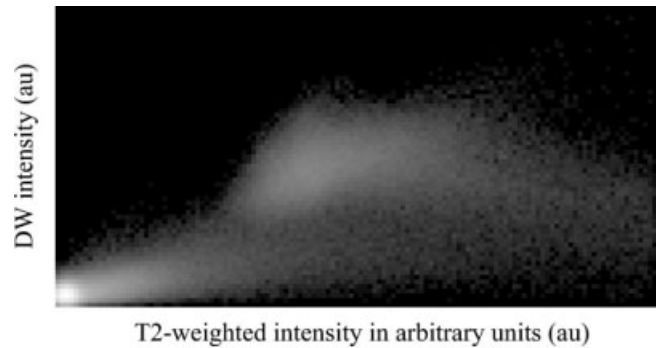

FIG. 2. Joint histogram showing the relationship between T_2-weighted and DW image intensities. The highly nonlinear nature of this relationship demonstrates why correlation type similarity measures are not appropriate for this application. Intensities are in arbitrary units.

mum variance. The second component is the normalized linear combination that is uncorrelated with the first component and whose variance is maximal, and so on. It turns out that the coefficients of such linear combinations are given by the characteristic vectors of the covariance matrix of **X** (22). As shown in the Results section, PCA is a powerful tool that can be used to detect interesting features in a DWI sequence, including artifacts such as image distortion and patient motion.

RESULTS

Cost Function

Figures 2 and 3 show that correlation type similarity measures are not appropriate for registering T_2-weighted and DW images. Correlation type similarity measures require signals in the target and source image to be linearly related. Figure 2, which displays the joint histogram of DW- and T_2-weighted images, shows that the intensity values of the images are not linearly related. This happens because cerebrospinal fluid (CSF) has low intensity in the DW images, but not in the T_2-weighted images. Consequently, background values in the DW images map to both background and CSF values in the T_2-weighted images. In addition, DW images contain signal affected by anisotropic diffusion, while the T_2-weighted images do not. As a consequence, white matter has a relatively narrow range of values in the T_2-weighted images but a large range of values in the DW images.

Figure 3 shows representative results for registration of a DWI to a corresponding T_2-weighted image using the correlation coefficient as well as the normalized mutual information as the similarity measure. The first (middle image) result was obtained using the normalized mutual information cost function. The image on the right was obtained using the correlation coefficient as a similarity measure. As evident from the picture, the result obtained using the mutual information cost function is superior to that obtained using the correlation coefficient. We note that the original DW images were acquired with gradient preemphasis turned off. Thus the original images contained significant geometric distortions. For brevity, the
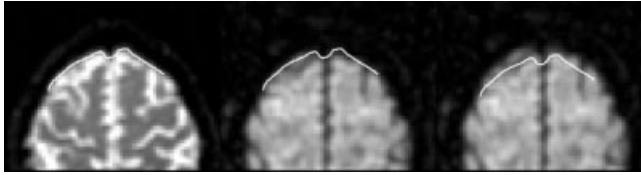
FIG. 3. Example image registrations performed using mutual information and correlation coefficient similarity measures. Left image: Reference T_2-weighted image. Middle image: DW image registered to the reference image using normalized mutual information. Right image: DW image registered to the reference image using the correlation coefficient similarity measure.

original distorted images are not shown here. Close visual inspection reveals that the edges of the brain shown in the images are well matched only when the normalized mutual information cost function is used. The use of the correlation coefficient causes the gray matter in the DW image to be matched to the CSF in the T_2-weighted image. Such visual inspections, which were initially performed to check the accuracy of our correction approach, revealed that the image distortion model described above appears to be appropriate for correcting relatively large distortions in images acquired with b-values of about 1100 mm²/s (which are typically used in clinical studies).

Adequacy of the Eddy Current-Induced Distortion Model

We tested whether the terms included in Eq. [12] were sufficient to approximate the distortions encountered in the image volume. We measured the distortion produced by x-, y-, and z-oriented diffusion gradients in each slice of the phantom using a 2D affine registration algorithm. The resulting correction coefficients for translation, magnification, and shear are plotted against the slice position in Fig. 4. The translation coefficient has dimensions of length and is measured in pixels; the magnification coefficient is unitless, representing the ratio between the size of the original and the corrected image; and the shear coefficient is expressed in pixels per column. Slice position zero denotes the isocenter of the magnet, and each slice is indexed in terms of its slice position (in millimeters). The gradient preemphasis scheme provided by the magnet manufacturer was turned off during the acquisition of these images, and consequently large corrections were necessary to register the DW images to the undistorted T_2-weighted image. With the exception of the first few slices, a quadratic function describes well the required correction as a function of slice position for all gradients, indicating that the terms included in Eq. [12] are sufficient to approximate the correction for distortions encountered in the image volume. The values of the correction coefficients for the first few slices differed significantly from those of the remaining slices. This suggests that the eddy-current field is not constant during the acquisition of the first few slices of a new DWI volume. In a separate experiment, we performed a single-slice measurement on a phantom in order to characterize the time course of the achievement of the steady state of the eddy current field for the x-, y-, and z-gradients. This experiment showed that, in our magnet for all gradients, reaching a steady state in the eddy-current field required about 500–750 ms when images were acquired with a TR of 250 ms. This result is in line with the findings of the multislice experiment described in Fig. 4. Identical experiments were performed using an image acquisition sequence in which the gradient preemphasis scheme was turned on. The results for these experiments were qualitatively equal to the ones shown, although the distortions measured were significantly smaller. For brevity, we do not report them here.

Intensity Correction

The effect of omitting the intensity correction step when significant distortions are present is shown in Fig. 5. Here a set of DW images with severe distortion were acquired by turning off the gradient preemphasis eddy-current compensation. These DW images were coregistered and aligned to the T_2-weighted image, and **D** was computed

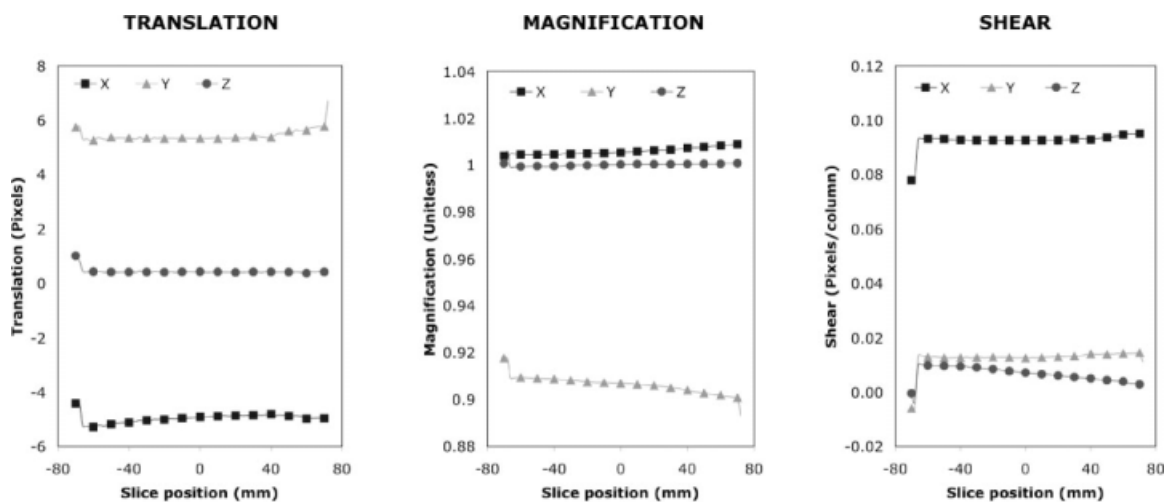FIG. 4. Study of image distortions using phantoms. Registration of DW images and a target T_2-weighted image was performed slice by slice using an affine transformation. The registration parameters (translation, shear, and scaling) for the DW images acquired with sensitizing gradients in the x-, y-, and z-directions are shown above.
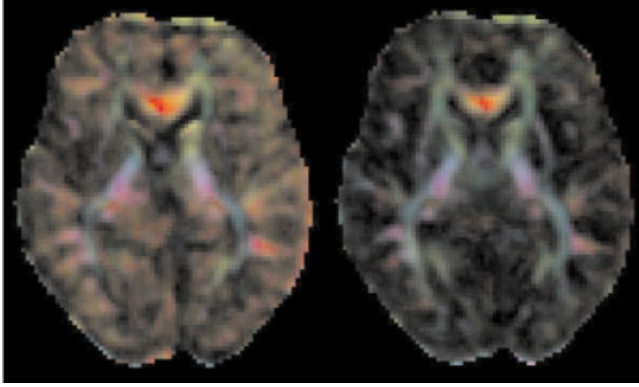
FIG. 5. Demonstration of artifacts introduced when the intensity values of the DW image are not recomputed after warping. Left image: Color representation of tensor maps computed from a DW image in which the intensity values were not recomputed after registration. Right image: The same as the left image, but with DW image intensity values properly recomputed. The background bias (red in the color image) seen on the left image appears to indicate preferential diffusion in the x-direction. The background artifacts disappear when appropriate correction is used.

from two sets of images: one with brightness correction and one without. Figure 5 shows the fiber orientation color maps (24) computed from diffusion tensors obtained from these two sets of images. In the color map computed from images that had no brightness correction (left image), a red background in isotropic regions is evident, indicating anisotropic diffusion in the left–right orientation. This artifact is completely removed in images in which the signal magnitude was appropriately corrected for the amount of nonrigid body distortion applied during image warping.

Subject Motion

To test the ability of our algorithm to correct for subject motion, we acquired a dataset in which the subject was asked to move his head deliberately three times (about 10° rotation to the left, about 10° rotation to the right, and an extension of about 10°). The resulting DW images in this dataset were significantly misaligned due to patient motion. Gradient preemphasis was turned on during this acquisition. Figure 6 contains maps of the relative anisotropy (25) computed in three representative slices from uncorrected images (top row) and images that were coregistered using our algorithm (bottom row). The relative anisotropy is a diffusion anisotropy index that corresponds to the coefficient of variation of the three eigenvalues of the diffusion tensor in each voxel (25). In the anisotropy maps computed from the uncorrected images, several white-matter structures that are clearly visible in the anisotropy maps computed from the registered images can not be identified. This is most evident in frontal regions where motion was most severe. In addition, the anisotropy maps computed from the uncorrected images show an artifactual rim of increased anisotropy around the periphery of the brain.

For the same dataset, Fig. 7 shows representative slices of the χ^2 maps produced by the tensor fitting procedure.

The top row contains the χ^2 maps of the original data prior to correction. The bottom row shows the χ^2 maps after correction. For display purposes (i.e., to increase the dynamic range of the displayed image and reveal more inner structure), the square root of χ^2 is shown. In this experiment, the mean χ^2 of the image was reduced by about 80% after correction with our approach. Note that the χ^2 maps' corrected datasets still contain slight bands of increased χ^2 in some regions of the brain. One possible explanation for the presence of these bands is that we did not remove the volumes acquired during the voluntary motion. In these volumes there is significant intravolume misregistration that our program does not correct for, which could account for these residual artifacts.

For the same dataset, Fig. 8 shows the coefficients for the first 16 principal components in each voxel for a DWI dataset corrected for misalignment. The coefficients of the components are displayed in order of decreasing variance, starting from the top left. The coefficients of the first two components shown in Fig. 8 appear to be related to T_2-weighted contrast from the different tissues, and to signal attenuation due to isotropic diffusion. The coefficients of components 4−8 clearly show effects related to anisotropic diffusion in white matter. Components 9 and higher show mostly noise. Figure 9 shows the same decomposition for DW images that have not been coregistered. Not only do the first few components appear blurred, but most components higher than 8 contain significant coefficient variability. For the PCA analysis of both registered and unregistered data, the volumes acquired when the voluntary motion occurred have been removed, and striations such as those observed in Fig. 7 are not visible. An interesting observation from the uncorrected dataset shown in Fig. 9 is that the features related to diffusion anisotropy and motion-induced artifacts do not separate into distinct components.
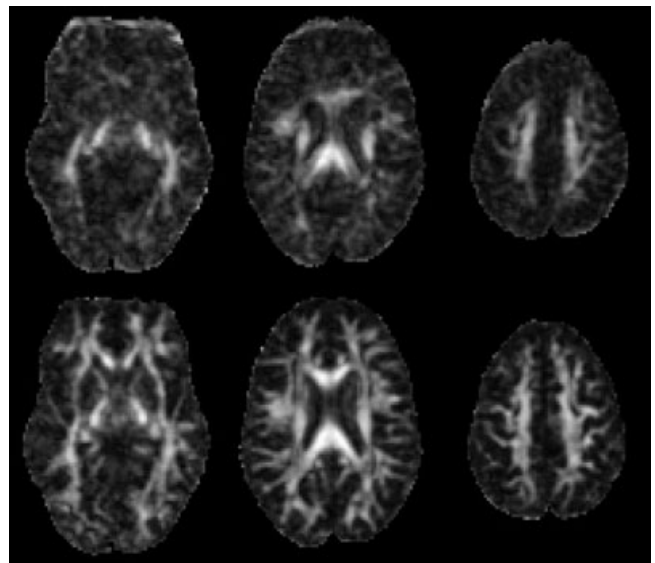

FIG. 6. Axial views of the relative anisotropy index for three representative slices. Top row: Anisotropy indexes computed from DW images without alignment. Bottom row: Anisotropy indexes computed from DW images corrected for alignment. Apparent anisotropy around the top edges of the images appears to be significantly reduced in the corrected images.
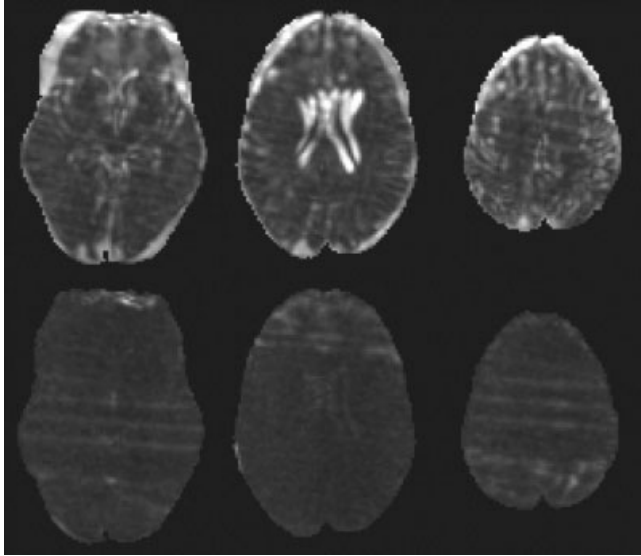
FIG. 7. Axial views of the fit of the diffusion tensor for three representative slices. Top row: Fit without alignment. Bottom row: Fit from DW images corrected for alignment. The chi-squared error between the ADT model and the DWI data is significantly reduced after motion and distortion correction, indicating better image alignment.

Figure 10 contains the plot of the relative variance of the coefficients of components 3–16 for the corrected and uncorrected datasets. The total variance (sum of the variances of each component) for a dataset was normalized to one for both datasets. The first two components account for 82% and 91% of the variance in the uncorrected and corrected DWI datasets, respectively. The plot shows that fewer principal components are required to describe the intensity signal in the DWI dataset after motion and distortion correction. This confirms that fewer sources of signal are present in the data after correction. Given that no qualitative loss in signal anisotropy was detected after correction, we conclude that the effects of sources related to image misalignment have been reduced after image registration.

DISCUSSION

We have presented a novel method for correcting image distortion and patient motion in DWI datasets. We use a mutual information-based registration algorithm to align each DWI volume in a dataset to a target volume chosen from the same DWI dataset. The registration is performed in 3D, and the warping function allows for rigid body patient motion as well as eddy current-induced distortion. All parameters are optimized simultaneously so that the final registration result represents an optimal correction of both patient motion and image distortion. After registration, the image intensity of each DWI volume is adjusted according to the spatial transformation applied to it. This prevents eddy current-induced distortions from introducing directional bias in the computed tensors. Similarly, each *b*-matrix is properly rotated using the same rotation applied to the corresponding DW image.

One of the novel aspects of our approach is the use of a model for eddy current-induced fields based on Laplace's equation. A derivation of the image distortion caused by such fields, as well as the brightness correction term necessary for adjusting the intensity values of the images, is also provided. Lastly, if desired, the target volume for the DWI dataset can first be registered to a template. Subsequent registration of the DW image to the target T_2-weighted volume will then cause the whole DWI dataset to be registered to a normalized template without additional computational cost, and with only one interpolation of the images. Thus our correction framework not only removes motion and distortion artifacts, but also positions the dataset in a standardized orientation using a single interpolation step. Note that although we designed our method for the purpose of spatially aligning DW images of the human brain, it can be easily adapted to work with other types of images. The method is relatively fast. Our code written in IDL (Research Systems Inc.) aligns each 3D volume of size $128 \times 128 \times 72$ in about 3 min on a Linux machine equipped with a 2 GHz Xeon processor. Implementing the method in a more efficient computer language, such as C, would certainly reduce the computation time for each image.

The results show a significant increase in data quality. Validation included visual inspection of the data, as well as more quantitative measures, such as the study of the χ^2 error of the fitting of the data to the **D** model. In addition, PCA decompositions were used to study the data variance introduced by image misalignment. All of the results presented show that the quality of the DW images datasets is significantly improved after alignment. When large distortions are present, it is necessary to remap the intensity values of the aligned DW image according to the Jacobian matrix of the transformation to avoid directional bias artifacts. When relatively small distortions are present, such artifacts are difficult to detect visually, even though the directional bias in the tensor field may still be present. The same can be expected for the *b*-matrix rotation step. If significant patient motion is present, it is essential to rotate the *b*-matrix to avoid erroneous computation of diffusion parameters.

Patient motion and eddy current-induced image distortion are common problems in clinical DWI acquisitions. Gradient preemphasis schemes that are currently implemented in most MRI scanners are very effective in reducing the impact of eddy currents. In our scanner, eddy current-induced distortions rarely exceed one or two pixels when preemphasis correction is applied. However, gradient preemphasis must be calibrated periodically. Datasets acquired immediately after calibration will have fewer artifacts than those acquired when a long period of time has elapsed since calibration. This temporal inconsistency in the quality of DWI data may be problematic in longitudinal studies and in general when the ability to compare scans acquired over time is desired. In our clinical studies, the systematic use of our correction scheme significantly increased the reproducibility of our clinical diffusion studies. In our experience, misalignment artifacts caused by patient motion are more problematic, especially in lengthy acquisitions where several DW images are needed, or even in short scans with uncooperative patients or with
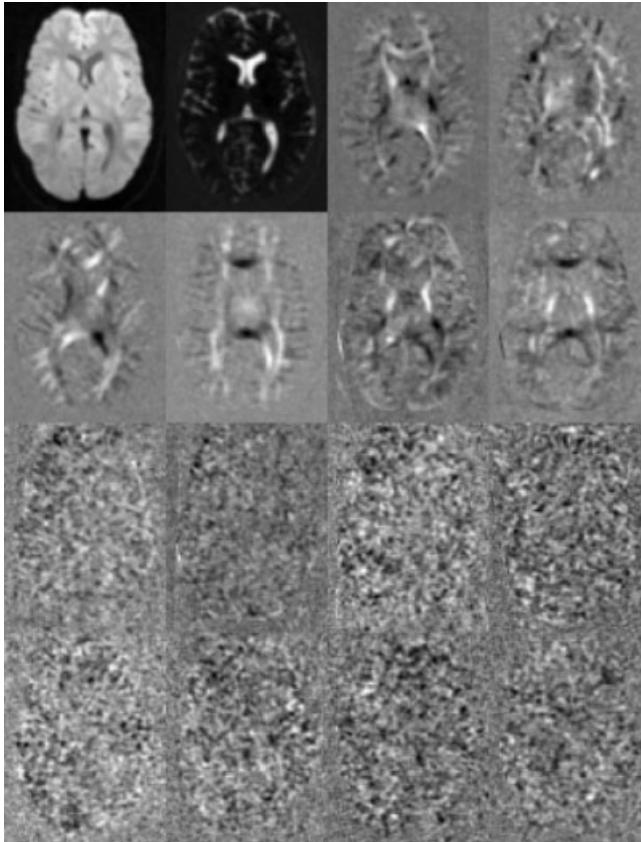
FIG. 8. PCA decomposition of the registered DWI dataset (first 16 components). Images are displayed in order of decreasing variance, starting from the top left. Image variance around the edges of the brain and in the CSF–white matter interfaces, appears to be reduced in the third and fourth components.

unsedated pediatric subjects. Our results show that datasets containing significant motion can be successfully corrected.

Our DWI normalization method is still unable to correct some motion artifacts that can be present in DWI acquisitions. We perform a 3D registration between brain volumes, rather than a 2D registration between individual slices. Given that the 3D volumes are assembled from separate slice acquisitions, there may be patient motion from one slice acquisition to another that will be uncorrected by our approach. We chose to perform a 3D registration because it is generally more robust than a 2D registration. Moreover, with a 2D registration, correcting for in-plane motion is feasible, but correcting for out-of-plane motion is much more difficult. With our approach we can correct for some types of out-of-plane motion; for example, in axial images we can correct for translations in the z-axis and rotations about the x- and y-axes. We also tested the possibility of performing the 3D registration first, followed by a 2D registration to correct for in-plane motion between slices. However, we did not find that this strategy led to a significant improvement in the alignment of the images. Clearly, the order of data acquisition is very important for a 3D approach to be effective: all slices

composing a volume should be acquired in the shortest possible time. One additional problem is that the human brain is not strictly a rigid structure, and cardiac-induced motion may also deform the brain in ways that we are not currently able to account for with our model. We are attempting to characterize the amount of image misalignment due to cardiac pulsation so that we can devise appropriate correction methods.

Finally, we anticipate that the algorithm presented here may not be able to properly register images acquired with diffusion weighting much higher than that used in this study ($b = 1100$ s mm^{-2}). At very high b-values, the image signal in the brain parenchyma is significantly attenuated, so it may be confounded with signal from the air, nearly eliminating tissue/air boundaries that are some of the main features that guide the image registration process. Under these circumstances, the probability density functions (intrinsic contrast) of T_2-weighted and DW images is too dissimilar, and even a mutual information-based registration algorithm would fail. One possible solution to this problem would be to perform image registration in a sequential or hierarchical manner. Rather than registering each heavily weighted DWI volume to a reference T_2-weighted volume, one can obtain intermediate images that have more
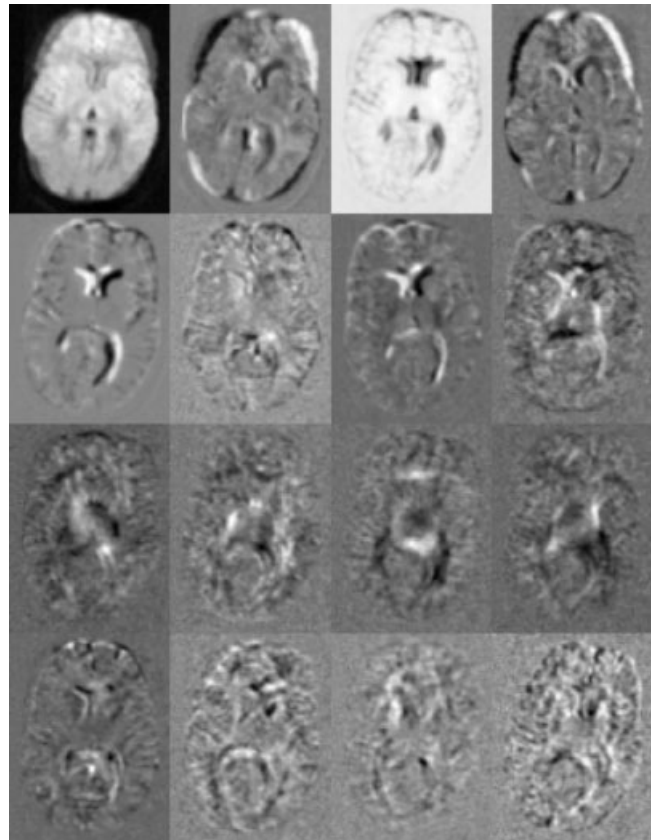

FIG. 9. PCA decomposition of an unregistered DWI dataset (first 16 components). Images are displayed in order of decreasing variance, starting from the top left. Data variance around the edges of the images and in the CSF–white matter interfaces is apparent in nearly all components.

Relative Principal Component Variance

FIG. 10. Relative variance of principal components, starting from the third component, for both registered and unregistered DWI datasets. The relative variances of the third and fourth components are reduced in the corrected dataset.
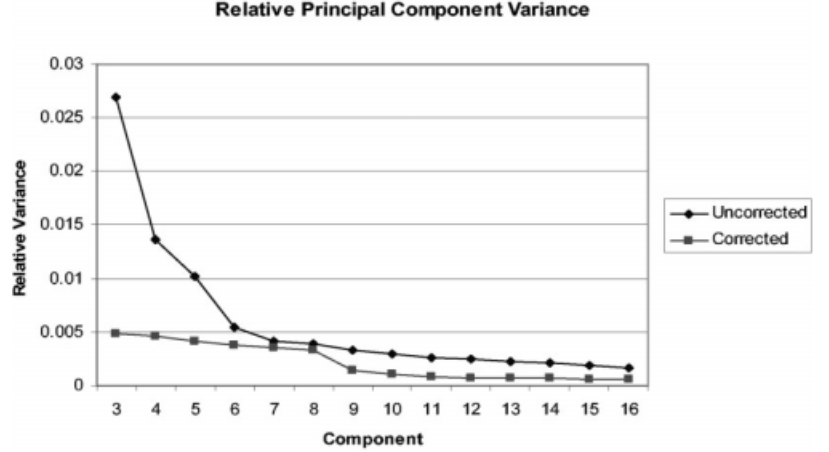
similar probability density functions and are thus easier to register. For example, replicate volumes acquired with the same strength and orientation of the diffusion gradients can first be registered among themselves (with a rigid body transformation) and averaged to increase SNR. The next step would be to obtain "trace-weighted" volumes with improved SNR and anisotropy information removed. Compared to the original DWI volumes, trace-weighted volumes will have a probability density function more similar to that of T_2-weighted volumes. Trace-weighted volumes can be obtained by computing the geometric average of a set of volumes acquired using b-matrices that must have certain properties (see Ref. 27 for more details on how to compute a trace-weighted DWI). Volumes obtained from the first averaging step can be registered among themselves and geometrically averaged. The resulting trace-weighted volume with the lowest b-value can in turn be registered to the T_2-weighted volume, becoming the reference image for the trace-weighted volume with the second lowest b-value. This process can be repeated to register all trace-weighted volumes up to the highest b-value, achieving the goal of always registering volumes with similar contrast. The various transformations involved in this process can be combined and applied to each original DWI volume, avoiding artifacts originating from sequential interpolations. We are currently testing this approach, and we hope that it will extend the ability of our method to register heavily DW images.

APPENDIX

Derivation of Eq. [8]

Assuming that $b_{eddy}(\mathbf{y}_\alpha,t)$ is approximately constant during the readout and in steady state for the acquisition of different slices, the pixel values for volume α are

$$I_\alpha(m, l, q) = \sum_{n=-N/2}^{N/2-1} \exp\left(-i\frac{2\pi mn}{N}\right) \sum_{p=-P/2}^{P/2-1} \exp\left(-i\frac{2\pi lp}{P}\right)$$

$$\times \int_{-\infty}^{\infty} dy_{\alpha1} \int_{-\infty}^{\infty} dy_{\alpha2} W(y_{\alpha1}, y_{\alpha2}, qs_{\alpha3}) \exp(i(\phi_1 + \phi_2)) \quad [\text{A.1}]$$

where W is the magnetization density of the object, $\phi_1 = \gamma G_1 y_{\alpha1}$, $\phi_2 = \gamma(G_2 y_{\alpha2} + b_{eddy}(\mathbf{y}_\alpha)\tau_{echo})$, and G_1 is the product of the readout gradient and the sample time, and G_2 is the area of the phase-encode blip. The value of the double integral in Eq. [A1] is the measurement raw data in slice q for readout point n and phase-encode p, and the double sum is the discrete Fourier transform in the reconstruction. Exchanging the order of the sums and the integrals, and regrouping, Eq. [A1] becomes

$$I_\alpha(m, l, q) = \int_{-\infty}^{\infty} dy_1 \int_{-\infty}^{\infty} dy_2 W(y_{\alpha1}, y_{\alpha2}, qs_{\alpha3})$$

$$\times \sum_{n=-N/2}^{N/2-1} \exp(-in\Phi_1) \sum_{p=-P/2}^{P/2-1} \exp(-ip\Phi_2) \quad [\text{A.2}]$$

where $\Phi_1 = \gamma G_1(y_{\alpha1} - ms_1)$, $s_1 = 2\pi/N\gamma G_1$, is the pixel size in the y_1 direction, $\Phi_2 = \gamma G_2(y_{\alpha2} + \beta b_{eddy}(\mathbf{y}_\alpha) - ls_2)$, $s_2 = 2\pi/P\gamma G_2$ is the pixel size in the y_2 direction, and

$$\beta = \frac{\tau_{echo}}{G_2}. \quad [\text{A.3}]$$

The sums in Eq. [A2] can be evaluated analytically (26), transforming Eq. [A2] into

$$I_\alpha(m, l, q) = \int_{-\infty}^{\infty} dy_{\alpha1} \int_{-\infty}^{\infty}$$

$$\times \; dy_{\alpha2} W(y_{\alpha1}, y_{\alpha2}, qs_{\alpha3}) H_N(\Phi_1) H_P(\Phi_2) \quad [\text{A.4}]$$

where

$$H_N(\Phi) = \exp\left(i\frac{\Phi}{2}\right) \frac{\sin(N\Phi/2)}{\sin(\Phi/2)}. \quad [\text{A.5}]$$

$H(\Phi)$, the PSF of the acquisition, is large only close to the points where the denominator vanishes. The contribution to the integral from the lines centered at $\Phi \neq 0$ is wrapped

around due to aliasing and vanishes if the FOV is large enough. To evaluate the integrals in Eq. [A4], we perform he change of variables

$$x_{\alpha 1} = y_{\alpha 1} - ms_1 \qquad [A.6]$$

$$x_{\alpha 2} = y_{\alpha 2} + \beta b_{eddy}(\mathbf{y}_\alpha) - ls_2 \qquad [A.7]$$

which transforms Eq. [A4] into

$$I_\alpha(m, l, q) = \int_{-\infty}^{\infty} dx_{\alpha 1} \int_{-\infty}^{\infty} dx_{\alpha 2} W$$

$$\times (x_{\alpha 1} + ms_1, y_{\alpha 2}(\mathbf{x}_\alpha), qs_{\alpha 3}) J(\mathbf{x}_\alpha) H_N(\gamma G_1 x_{\alpha 1}) H_P(\gamma G_2 x_{\alpha 2}) \quad [A.8]$$

where $J(\mathbf{x}_\alpha) = \left| \dfrac{\partial(y_{\alpha 1}, y_{\alpha 2})}{\partial(x_{\alpha 1}, x_{\alpha 2})} \right|$ Jacobian determinant of the inverse of transformation [A6] and [A7], and $y_{\alpha 2}(\mathbf{x}_\alpha)$ is computed from Eq. [A7]. If we view H(Φ) as an approximation of a dirac delta function, Eq. [A7] tells us that the measured image $I_\alpha(m,l,q)$ is the true image shifted in the x_2-direction and weighted by the Jacobian determinant. If the distortion is small compared to the distance over which b_{eddy} changes appreciably, the inverse of Eq. [A7] can be approximated as

$$y_{\alpha 2} = x_{\alpha 2} - \beta b_{eddy}(\mathbf{x}_\alpha) + ls_2 \qquad [A.9]$$

with

$$b_{eddy}(\mathbf{x}_\alpha) \cong b_{eddy}(\mathbf{y}_\alpha). \qquad [A.10]$$

The Jacobian then becomes

$$J = 1 + \frac{\partial(\beta b_{eddy})}{\partial x_2} \cong 1 + \frac{\partial(\beta b_{eddy})}{\partial y_2}, \qquad [A.11]$$

and Eq. [A8] can be written as

$$I_\alpha(m, l, q) = \tilde{W}_\alpha(ms_1, ls_2 - \beta b_{eddy}(ms_1, ls_2, qs_3), qs_3)$$

$$\times \left(1 + \frac{\partial(\beta b_{eddy})}{\partial y_2} \right). \quad [A.12]$$

where the function $\tilde{W}_\alpha$ is the undistorted image of volume smoothed by the PSF.

REFERENCES

1. Basser PJ, Mattiello J, Lebihan D. MR diffusion tensor and imaging. Biophys J 1994;66:259–267.
2. Tuch DS, Weisskoff RM, Belliveau JW, Wedeen VJ. High angular resolution diffusion imaging of the human brain. In: Proceedings of the 7th Annual Meeting of ISMRM, Philadelphia, 1999. p 321.
3. Wedeen VJ, Reese TG, Tuch DS, Weigel MR, Dou J-G, Weiskoff RM, Chesler D, Mapping fiber orientation spectra in cerebral white matter with Fourier transform diffusion MRI. In: Proceedings of the 8th Annual Meeting of ISMRM, Denver, 2000. p 82.
4. Inglis BA, Bossart EL, Buckley DL, Wirth III ED, Mareci TH. Visualization of neural tissue water compartments using biexponential diffusion tensor MRI. Magn Reson Med 2001;45:580–587.
5. Frank LR. Characterization of anisotropy in high angular resolution diffusion-weighted MRI. Magn Reson Med 2002;47:1083–1099.
6. Roemer PB, Hickey JS, inventors. General Electric Company, Milwaukee, WI, assignee. Self-shielded gradient coils for nuclear magnetic resonance imaging. U.S. patent 4,737,716; 1988.
7. Glover GH, Pelc NJ, inventors. General Electric Company, Milwaukee, WI, assignee. Method for magnetic field gradient eddy current compensation. U.S. patent 4,698,591; 1987.
8. Jezzard P, Barnett AS, Pierpaoli C. Characterization of and correction for eddy current artifacts in echo planar diffusion imaging. Magn Reson Med 1998;39:801–812.
9. Haselgrove JC, Moore JR. Correction for distortion of echo-planar images used to calculate the apparent diffusion coefficient. Magn Reson Med 1996;36:960–964.
10. Bastin ME. Correction of eddy current-induced artifacts in diffusion tensor imaging using iterative cross-correlation. Magn Reson Imaging 1999;17:1011–1024.
11. Horsfield MA. Mapping eddy current induced fields for the correction of diffusion-weighted echo planar images. Magn Reson Imaging 1999; 17:1335–1345.
12. Andersson JLR, Skare S. A model-based method for retrospective correction of geometric distortions in diffusion-weighted EPI. Neuroimage 2002;16:177–199.
13. Press WH, Teukolsky SA, Vetterling WT, Flannery BP. Numerical recipes in C. New York: Cambridge University Press; 1994.
14. Goldstein H. Classical mechanics. Reading, MA: Addison-Wesley; 1950. p 107ff.
15. Smyth WR. Static and dynamic electricity. 3rd ed. New York: McGraw-Hill; 1968.
16. Kullback S. Definition of information. In: Information theory and statistics. New York: Dover; 1968. p 1–11.
17. Viola P, Wells III WM. Alignment by maximization of mutual information. In: Proceedings of the 5th International Conference on Computer Vision, Boston, 1995. p 16–23.
18. Wells III WM, Viola P, Atsumo H, Nakajima S, Kikinis R. Multi-modal volume registration by maximization of mutual information. Med Imaging Anal 1996;1:35–51.
19. Maes F, Collignon A, Vandermeulen D, Marcha G, Suetens P. Multimodality image registration by maximization of mutual information. IEEE Trans Med Imaging 1997;16:187–198.
20. Studholme C, Hill DLJ, Hawkes D. Automated three-dimensional registration of magnetic resonance and positron emisson tomography brain images by multiresolution optimization of voxel similarity measures. Med Phys 1997;24:25–35.
21. Studholme C, Hill DLG, Hawkes DJ. An overlap invariant entropy measure of 3D medical image alignment. Intern J Pattern Recognit Artif Intell 1999;32:71–86.
22. Anderson TW. Principal components. In: Anderson TW, editor. An introduction to multivariate statistical analysis. New York: John Wiley & Sons; 1957. p 451.
23. Pierpaoli C, Jezzard P, Basser PJ, Barnett A, Di Chiro G. Diffusion tensor MR imaging of the human brain. Radiology 1996;201:637–648.
24. Pajevic S, Pierpaoli C. Color schemes to represent the orientation of anisotropic tissues from diffusion tensor data: application to white matter fiber tract mapping in the human brain. Magn Reson Med 1999;42:526–540.
25. Basser PJ, Pierpaoli C. Microstructural and physiological features of tissues elucidated by quantitative-diffusion-tensor MRI. J Magn Reson B 1996;111:209–219.
26. Abramowitz M, Stegun IA. Handbook of mathematical functions. New York: Dover; 1974. p 10.
27. Basser PJ, Jones DK. Diffusion-tensor MRI: theory, experimental design and data analysis—a technical review. NMR Biomed 2002;15:456–467.